Nanoscale

Accepted Manuscript

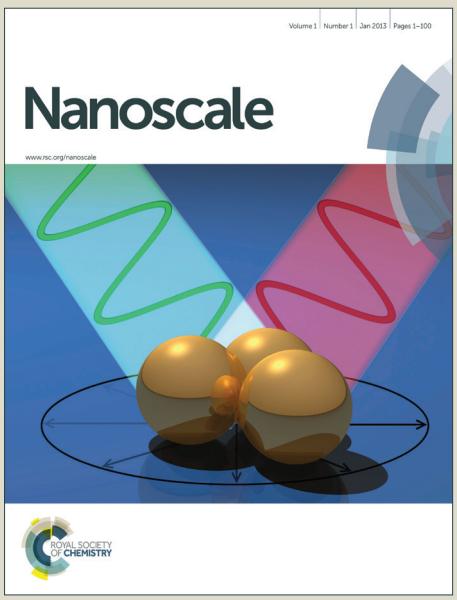

ROYAL SOCIETY OF CHEMISTRY

www.rsc.org/nanoscale

Multifunctional superparamagnetic nanoshells: combing two-photon luminescence imaging, surface-enhanced Raman scattering and magnetic separation

Xiulong Jin,[†] Haiyan Li,[†] Shanshan Wang,[†] Ni Kong,[†] Hong Xu,[†] Qihua Fu,[‡] Hongchen Gu,[†] and Jian Ye[†,]*

[†]Shanghai Engineering Research Center of Medical Device and Technology at Med-X, School of Biomedical Engineering, Shanghai Jiao Tong University, 1954 Huashan Road, Shanghai, 200030, China;[‡]Department of Laboratory Medicine, Shanghai Children's Medical Center & School of Medicine, Shanghai Jiao Tong University, Shanghai, 200127, China

RECEIVED DATE (to be automatically inserted after your manuscript is accepted if required according to the journal that you are submitting your paper to)

[*]To whom correspondence should be addressed. E-mail: yejian78@sjtu.edu.cn

ABSTRACT

With the increasing needs of multi-purpose analysis in biomedical field, traditional single diagnosis method cannot meet the requirements. Therefore new multifunctional technologies and materials for the integration of sample collection, sensing and imaging are in great demand. Core-shell nanoparticle offers a unique platform to combine multifunctions in a single particle. In this work, we have constructed a novel type of core-shell superparamagnetic nanoshells (Fe_3O_4@SiO_2@Au), composed of a Fe_3O_4 cluster core, a thin Au shell and a SiO_2 layer in between. The obtained multifunctional nanoparticles combine the magnetic properties and plasmonic optical properties effectively, which were well investigated by a number of experimental characterizations and theoretical simulations. We have demonstrated that Fe_3O_4@SiO_2@Au nanoparticles can be utilized for two-photon luminescence (TPL) imaging, near-infrared surface-enhanced Raman scattering (NIR SERS) and cells collection by magnetic separation. The TPL intensity could be further greatly enhanced through the plasmon coupling effect in the self-assembled nanoparticle chains, which were triggered by an external magnetic field. In addition, Fe_3O_4@SiO_2@Au nanoparticles may have great potential applications such as enhanced magnetic resonance imaging (MRI) and photo-thermotherapy. Successful combining multifunctions including magnetic response, biosensing and bioimaging in single nanoparticles allows further manipulation, real-time tracking, and intracellular molecule analysis of live cells at a single-cell level.

KEYWORDS: core-shell, plasmon, nanoshells, surface-enhanced Raman scattering, two-photo luminescence, superparamagnetic

With the increasing multi-target analysis needs in biomedical field, traditional single diagnosis method can never meet the requirements, and new multifunctional technologies and materials for the integration of sample collection, sensing and bioimaging are in great demand.[1-4] Multifunctional nanoparticles, compared to traditional single functional nanoparticles, can achieve the combination of multi-purposes, such as multimodal bioimaging (e.g. fluorescence imaging, magnetic resonance imaging (MRI), photoacoustic imaging), sensing, targeting, drug delivery and thermotherapy, which exhibit great potential for optimized therapy through personalized medicine.[5-7] Recently, multifunctional nano-particles with different geometries have been prepared including dimer, Janus and star shape, and porous structure.[8-11] Core-shell nanoparticles have attracted more interests for its geometrical advantages, which can offer a combination of multifunctions within different layers in a single nanoparticle and satisfy the demands of multifunctional purpose.[12-15] For instance, by adopting the selective etching method, a yolk-shell silica structure with controllable void space for drug delivery can be achieved; when modified with fluorescein isothiocyanate molecules, the obtained nanoparticles showed excellent biocompatibility, sustained anticancer drug release and imaging properties.[15] Moreover, the shell layer of core-shell nanoparticles can protect instable core components and improve the dispersity and biocompatibility of nanoparticles.[15, 16] For investigating the biological information during physiological processes in live cells, one has used the nanoparticle-based localized sensing technique for analyzing the biochemical composition or pH value in single cells and the high-spatial real-time bioimaging method for studying the functions of motor proteins.[17-19] Combination of such sensing and bioimaging capability into single nanoparticles is therefore highly of interest, because they may allow further long-term real-time tracking and intracellular molecule analysis of live cells.

Two-photon luminescence (TPL) imaging technology has become one of the most powerful bioimaging tools for biological analysis since it was first introduced in 1990.[20-22] TPL is an optical process that the luminophores are excited by simultaneous absorption of two near-infrared (NIR) photons and emit a high energy single photon in visible spectrum.[23] Therefore, TPL imaging shows great advantages compared to traditional luminescent imaging techniques in visible spectrum for its large tissue penetration depth and reduced photo-damage. In contrast to the conventional fluorescent dyes, metallic plasmonic nanostructures (e.g. Au nanoparticles) also present TPL emission properties and the phenomena are remarkably enhanced when plasmonic nanoparticles are excited by a femto-second pulsed laser in resonance with their plasmon modes.[24-26] In the TPL process, plasmonic nanostructures simultaneously absorb two photons to excite the electron from *d*-band to *s-p* band, creating electron-hole pairs. In the subsequent relaxation process, due to the recombination of electron-hole pairs, luminescence is emitted in the visible range.[27, 28] When compared with organic dyes, single plasmonic nanoparticles may produce ~10^6 times greater signal compared to a single dye molecule and are not as susceptible to photo-bleaching, showing a much better stability.[29] Recently TPL has been used to demonstrate the *in vitro* imaging capability with the employment of Au nanoshells and nanocages.[30-33] For example, the visualized TPL imaging of nanoshells distribution in tumor and other critical organs has provided a unique way to study the accumulation kinetics of Au nanoparticles *in vivo*.[30] Additionally, plasmonic photothermal therapy effect can be further combined with TPL imaging for the examination and treatment of cancer cells.[31, 34-37]

Surface-enhanced Raman scattering (SERS) effect amplifies the Raman signals of adsorbed molecules on the surface of noble metallic nanostructures when their plasmon resonances and consequently enhanced near-fields are excited by the stimulating laser beam. The enhancement of SERS

may reach a level of single-molecule resolution, and therefore it has been extensively explored in many biomedical applications such as biosensing and bioimaging.[38-40] By combing rapid detection and high sensitivity of the SERS effect, the obtained multifunctional nanoparticles could be used to real-time analyze the biochemical composition inside a living cell and to monitor chemical reaction. [17, 41-43] Due to the strong plasmon coupling between the inner and outer surface of the Au shell layer, Au nanoshells have exhibited highly tunable optical properties from the visible to NIR optical region and have been considered as an ideal NIR SERS substrate.[44-48] For example, by measuring SERS signals under nanoshells fabricated SERS substrate, the primary DNA base modifications such as methylation of adenine, methylation and hydroxymethylation of cytosine, and guanine oxidation could be identified successfully, providing a simple and direct method for clinical diagnostics.[48]

In this article, we constructed a new kind of multifunctional superparamagnetic plasmonic nanoshells (Fe_3O_4@SiO_2@Au) to combine the capabilities of bioimaging, sensing and magnetic response. The multifunctional nanoparticles were composed of a core of iron oxide (Fe_3O_4) cluster, a thin shell of Au, and a silica (SiO_2) layer in between. The plasmonic properties of the Au shell offer the capabilities of TPL imaging and SERS-based sensing. The superparamagnetic Fe_3O_4 cluster cores allow the particle manipulation and sample collections by an external magnetic field. Extensive characterization tools and simulation method including transmission electron microscopy (TEM), zeta-potential measurement, superconducting Quantum Interference Device (SQUID) magnetometer, UV-Vis spectrometer, and finite difference time domain (FDTD) simulation have been applied to well investigate the morphology, magnetic and optical properties of Fe_3O_4@SiO_2@Au nanoparticles. We have additionally studied how the nanoparticle chains self-assembled under the magnetic field influence the TPL intensity.

Experimental

Materials. Ethanol, ethylene glycol, isopropanol, ammonium hydroxide aqueous solution (25–28 wt.%), sodium chloride, sodium hydroxide, potassium carbonate, urea, ferric chloride hexahydrate ($FeCl_3 \cdot 6H_2O$, 99%), tetraethyl orthosilicate (TEOS), chloroauric acid tetrahydrate ($HAuCl_4 \cdot 4H_2O$), and formaldehyde aqueous solution (37–40%) were purchased from Sinopharm Chemical Reagent Co. (Shanghai, China). Poly(acrylic acid) (50 wt.% solution in water, MW≈5000) was obtained from ACROS (Beijing, China). 3-Aminopropyl-triethoxysilane (APTES, 99%) and 4-mercaprobenzoic acid (4-MBA, 99%) were obtained from Aladdin (Shanghai, China). Tetra(hydroxymethyl)phosphoniumchloride (THPC, 80 wt.% solution in water) was purchased from TCI (Tokyo, Japan). All chemicals were used as received without further treatment. Deionized water (18.2 MΩ) was provided by a CascadaTM system.

Synthesis of Fe_3O_4@SiO_2@Au. Fe_3O_4 cluster cores were synthesized by the solvent-thermal method[49] with an average diameter of 74 nm and the detailed procedure has been described before.[50] The prepared Fe_3O_4 cores were coated with a thin SiO_2 layer via a modified Stöber reaction.[51] In a typical synthesis, 12 mg Fe_3O_4 nanoparticles were suspended in a mixture solution of 3 mL deionized water and 20 mL ethanol, then 0.5 mL aqueous ammonia was added quickly during mechanical stirring. 50 μL TEOS was diluted by 50 μL ethanol, and then added dropwise to the mixture. After reaction for 12 h at room temperature, the obtained Fe_3O_4@SiO_2 nanoparticles were collected by an external magnetic field and were washed twice with ethanol, then transferred to 20 mL isopropanol. 50 μL APTES was then added into the solution and the mixture was kept at 80 °C with mechanical stirring for 2 h. The resulting particles were functionalized with amino groups on the silica surface. After washing twice with

isopropanol, the surface modified particles were dispersed in 5 mL deionized water. THPC Au solution composed of 1 – 2 nm Au colloids was prepared as reported in the literature and stored for a minimum of 2 weeks before usage.[52, 53] Au plating solution was prepared by following the process developed previously and stored for at least 2 days.[53] Seeds were obtained by mixing surface-modified Fe_3O_4@SiO_2 nanoparticles and THPC gold solution. Next, 50 mL THPC Au solution was mixed with 1.25 mL 1M NaCl, then 2.5 mL surface modified Fe_3O_4@SiO_2 nanoparticles were added into the mixture and the resulting solution was allow to reach equilibrium over 12 h. The obtained seeds were collected by an external magnetic field and were washed with deionized water, then dispersed into 20 mL deionized water. Finally, Fe_3O_4@SiO_2@Au nanoparticles were obtained by adding 150 μL formaldehyde into the mixture of 0.6 mL seeds and 30 mL Au plating solution. Before storage, particles were washed twice with deionized water and dispersed into 10 mL deionized water.

Functionalization of Fe_3O_4@SiO_2@Au with 4-MBA. Without washing, the final product of Fe_3O_4@SiO_2@Au nanoparticles obtained above were mixed with 400 μL 10 mM 4-MBA ethanol solution and sonicated for 5 min. The resulting products were separated by centrifuging at 3000 rcf, washed twice with ethanol to remove excess 4-MBA, and finally dispersed in 10 mL deionized water.

Cell culture. The human umbilical vein endothelial cells (HUVECs) were obtained from human umbilical cord vein according to previous work.[54] The cells were cultured on culture plates with endothelial cell medium (ECM, Sciencell) under 5% CO_2 at 37 °C for 4 days. HUVECs were seeded in 6 mL culture plate at a population of 3×10^5 cells. Cell culture medium was refreshed before the cells were incubated with Fe_3O_4@SiO_2@Au nanoparticles. Then, Fe_3O_4@SiO_2@Au nanoparticles were

added into culture plate at a final concentration of 0.02 nM and incubated for 24 h. For two-photon confocal imaging experiments, after incubation, culture medium was removed and the cells were rinsed with phosphate buffered saline (PBS) buffer solution twice before being fixed with 4% paraformaldehyde for 10 min. The fixed cells were washed with deionized water to remove excess paraformaldehyde, and then were directly used in two-photon confocal imaging experiments under deionized conditions. For magnetic separation experiments, the cells were trypsinized and separated by an external magnetic field (Magical Trapper, Toyobo). The magnetic separation efficiency was calculated by the method of cell counting.

Instrumentation. UV–Vis spectrometer studies were carried out using a Unicam UV 300 spectrometer (Thermo Fisher, USA) with a slit width of 2 nm and a data interval of 0.5 nm. TEM images of the nanoparticles were obtained using a JEOL-2010 transmission electron microscope (JEOL, Japan) operating at 300 kV. Zeta potential measurements were taken with Malvern Zetasizer Nano ZS. Superconducting Quantum Interference Device (SQUID) magnetometer (Quantum Design, USA) was used to characterize the magnetic properties of our nanoparticles. Confocal TPL imaging was performed in a Nikon A1R MP microscope system, coupled with a 60× water immersion objective with a numerical aperture (NA) of 1.1. For TPL imaging experiments, the HUVECs labeled with Fe_3O_4@SiO_2@Au were excited at 800 nm with a laser power of ~2 mW and the emission was collected with a channel of 601–657 nm. Transmission images were excited by a 488 nm laser (40 μw) and collected with a diascopic detector. To obtain TPL 3D images of cells (labeled with Fe_3O_4@SiO_2@Au nanoparticles), a step of 2 μm was taken during the scanning of Z direction. Raman spectra were obtained using an instrument of BrukerSenterra (50× objective, 0.5 NA) with a 785 nm laser (1 mW

power) or a 633nm laser (2 mW power) or a 532 nm laser (2 mW power). For Raman measurement, Fe_3O_4@SiO_2@Au nanoparticles were drop-casted on the Si substrate and dried before test. The spectral resolution of the system was less than 3 cm^{-1}. All Raman spectra were calibrated with the band of Si at 520 cm^{-1} and obtained with 10 s integration time.

Simulation. Numerical simulations were performed by employing a finite difference time domain (FDTD) method using the program of FDTD Solutions (Lumerical Solutions, Inc., Canada). The empirical dielectric functions of Au and Fe_3O_4 were fitted by Lumerical's multi-coefficient model (MCM).[55, 56] The simulation mesh size was set as 1 nm and the whole simulation region is set with a background index of 1.33 (water). For the sake of simplicity, the core of Fe_3O_4 clusters is considered as a single Fe_3O_4 nanoparticle with a same diameter.

Results and discussion

The entire fabrication process of superparamagnetic multilayered Fe_3O_4@SiO_2@Au core-shell nanoparticles was quite similar to that of nanoshells, and the detailed steps are depicted in Figure 1A. Fe_3O_4 clusters (i) prepared through a high-temperature hydrolysis reaction were protected by poly-(acrylic acid) (PAA),[49, 50] thus exhibiting good stability in aqueous solution. From a high resolution TEM image (the inset in Figure 1B), it can be seen that Fe_3O_4 clusters were composed of a great number of ~10 nm nanocrystals and exhibited a rather rough surface. Next, Fe_3O_4@SiO_2 nanoparticles (ii) were obtained by coating a thin SiO_2 layer around Fe_3O_4 clusters via a modified Stöber process. When coated with a SiO_2 layer, an obvious spherical core-shell structure was formed with a clear boundary between Fe_3O_4 core and SiO_2 layer and a relatively smooth surface (see Figure 1B). After the decoration by

APTES molecules under 80 °C in isopropanol,[57] Fe_3O_4@SiO_2 nanoparticles with a positively charged surface can be efficiently attached by 1—2 nm THPC Au sols via the electrostatic interaction. Compared to common decoration of APTES in ethanol at ambient temperature, heating in isopropanol can improve the surface density of the amino group and the cross-linking of SiO_2 layer. During this self-assembly process, 1 M NaCl solution was added to improve the ionic strength and consequently increase the density of THPC Au sols on the Fe_3O_4@SiO_2 surface. From the inset in Figure 1C, the attachment of a large number of 1—2 nm THPC protected Au sols on the surface of Fe_3O_4@SiO_2 nanoparticles could be clearly observed. Finally, Fe_3O_4@SiO_2@Au nanoparticles (iv) obtained through a seeded growth process under the reduction with formaldehyde were further purified and collected by an external magnetic field. Figure 1C shows that the Fe_3O_4@SiO_2@Au nanoparticles have a completed Au shell with a slightly rough surface. Additionally, a monolayer of 4-MBA molecules might be self-assembled on Fe_3O_4@SiO_2@Au nanoparticles to improve their dispersion and stability in aqueous solution. Figure 1D shows the size distribution of nanoparticles of Fe_3O_4 (i), Fe_3O_4@SiO_2 (ii), Au sols decorated Fe_3O_4@SiO_2 (iii) and Fe_3O_4@SiO_2@Au (iv) using statistic analysis method based on more than 150 nanoparticles for each of them from TEM images, indicating 76 ±13, 116±14, 125 ±12, and 178 ± 12 nm for their average diameters, respectively. With these examination results, the thickness of SiO_2 and Au layer can be estimated to be ~20 and ~30 nm, respectively. In order to further understand the modification of surface property during the preparation of nanoparticles, we performed the zeta potential measurement for nanoparticles. The results indicate the surface charge potential as -21.7, -24.8, -28.6 and -24.0 mV for nanoparticles (i) to (iv), respectively, which well explains the reason why they are all stable in aqueous solution.

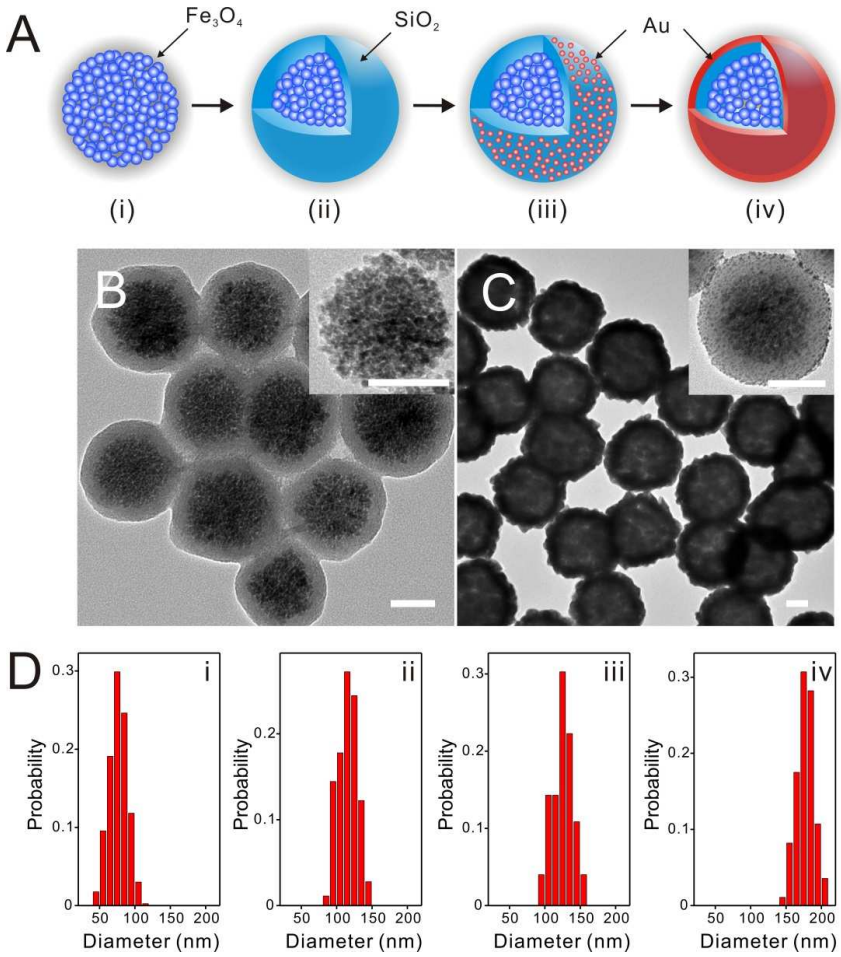

Figure 1. (A) Schematic illustration of the procedure for the fabrication of superparamagnetic Au nanoshells: (i) Fe_3O_4 clusters prepared through a high-temperature hydrolysis reaction; (ii) Fe_3O_4@SiO_2 nanoparticles obtained via a modified Stöber reaction; (iii) Au sols decorated Fe_3O_4@SiO_2 nanoparticles through the electrostatic interaction; (iv) Fe_3O_4@SiO_2@Au nanoparticles synthesized via a seeded growth method. (B) and (C) are TEM images of nanoparticles (ii) and (iv), respectively and the insets in (B) and (C) are TEM images of nanoparticles (i) and (iii), respectively. All scale bars are 50 nm. (D) Size distribution of nanoparticles (i) to (iv).

Figure 2A shows the hysteresis loop of Fe_3O_4 clusters measured by sweeping the external filed between -1.5 T and +1.5 T at room temperature (300 K). The results show that the saturated magnetization of Fe_3O_4 clusters is about 81 emu/g, which is similar to the results reported previously.[49] Observation of the negligible remanence implies the superparamagnetic behavior of Fe_3O_4 clusters at room temperature. This can be explained by the fact that each of Fe_3O_4 clusters is composed of small nanocrystals and the superparamagnetic property is retained after the formation of clusters. Figure 2B

shows that the superparamagnetic behavior of Fe_3O_4@SiO_2@Au nanoparticles is not affected but their saturated magnetization is reduced to about 4 emu/g, which is mainly due to the formation of SiO_2 and Au layer around the core of Fe_3O_4 clusters. The saturated magnetization of obtained multilayered nanoparticles can be further improved by decreasing the thickness of the SiO_2 and the Au layer if needed, for example, for the MRI application.

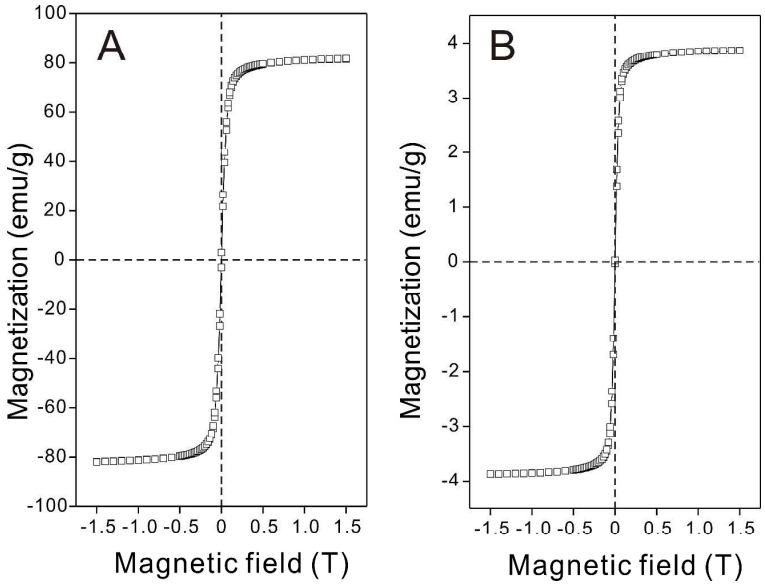

Figure 2. Magnetization curves of (A) Fe_3O_4 and (B) Fe_3O_4@SiO_2@Au.

The optical properties of superparamagnetic Fe_3O_4@SiO_2@Au nanoparticles were investigated by comparing their experimental extinction spectrum with theoretical one as seen in Figure 3. Figure 3A shows the experimental extinction spectrum of Fe_3O_4@SiO_2@Au nanoparticles in aqueous solution with a strong and broad peak centered at ~780 nm and a shoulder at ~610 nm. In contrast, the extinction spectrum of Fe_3O_4 clusters (dashed line in Figure 3A) exhibits remarkable decrease beyond 500 nm, which confirms that Fe_3O_4 cores have little effect on the plasmon resonance of Fe_3O_4@SiO_2@Au nanoparticles. To further investigate the detailed plasmonic behavior of Fe_3O_4@SiO_2@Au nanoparticles, we employ a finite difference time domain (FDTD) method to simulate their extinction

spectrum, local electric field enhancement and surface charge distribution. The simulated extinction spectrum of Fe_3O_4@SiO_2@Au nanoparticles was shown in Figure 3B displays two plasmon peaks at 763 (mode **1**) and 580 nm (mode **2**), which agrees well with the experimental spectrum. These two peaks correspond to a dipolar and a quadrupolar resonance mode, respectively, and have been confirmed by the local electric field enhancement and surface charge profiles calculations (see Figure 3C). In addition to the dipolar and quadrupolar characterization of electric field distribution on the surface of the outer shell, we can find that the field enhancement of mode **1** is much larger than that of mode **2**, which is similar to the optical properties of conventional nanoshells.[58, 59] This further demonstrates that plasmon resonances of the outer Au shell layer dominate the optical properties of multilayer core-shell nanoparticles. We have also observed the weak electric field enhancement near the Fe_3O_4 core, which is most likely attributed to the slight charge accumulation (see the right panels in Figure 3C) due to the image charge effect.[60, 61] We additionally note that experimental plasmon peaks are slightly broader than calculated ones. This can possibly be explained by the fact of polydispersed-particle-size induced inhomogeneous effect and the rough surface of the Au shell. By tuning the thickness of Au shell, the dipolar plasmon resonance of superparamagnetic Fe_3O_4@SiO_2@Au nanoparticles can be tuned from 700 nm to 900 nm as shown in Figure 3D, indicating a similar optical tunability like Au nanoshells.[62]

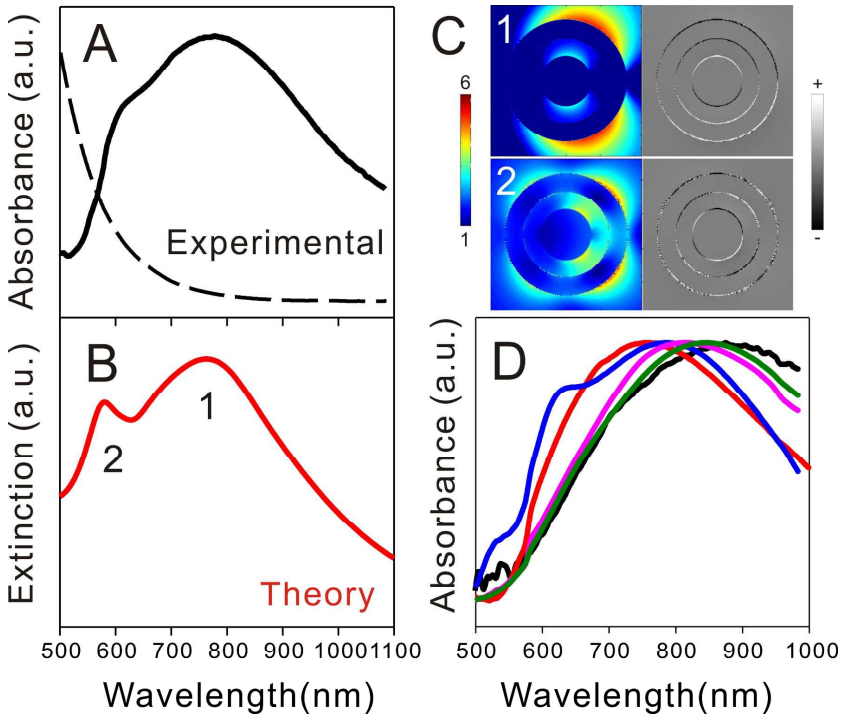

Figure 3. (A) Experimentally measured and (B) theoretically calculated extinction spectra of Fe_3O_4@SiO_2@Au nanoparticles in water. Dashed line in panel A is the measured extinction spectrum of Fe_3O_4@SiO_2 nanoparticles in water. (C) The calculated local electric filed enhancement (left) and surface charge distribution (right) of a Fe_3O_4@SiO_2@Au nanoparticle for the plasmon modes 1 and 2. Light is incident from left and the polarization is along the vertical direction. (D) Normalized extinction spectra of Fe_3O_4@SiO_2@Au nanoparticles with tunable plasmon resonances in the near-infrared range.

To examine the TPL imaging capability of Fe_3O_4@SiO_2@Au nanoparticles, we incubated nanoparticles with HUVECs at 37°C for 24 h without addition of any dye or other labeling molecules. Figure 4A shows the bright field image of HUVECs cultured without Fe_3O_4@SiO_2@Au nanoparticles, where the spindle HUVECs can be seen clearly when adhering to the culture plate. When HUVECs were cultured with Fe_3O_4@SiO_2@Au nanoparticles for 24 h, the nanoparticles could be taken up by cells effectively through endocytosis process with an undecorated particle surface (Figure 4B). Partially enlarged bright field image of Figure 4B in the blue circle region containing several HUVECs reveals the accumulation of superparamagnetic Fe_3O_4@SiO_2@Au nanoparticles around the cell nucleus, which is similar to the results in previous work reported by Xin Nie *et al.*.[63] Moreover, an enlarged

transmission image of a single HUVEC in Figure 4C further confirms the observation of nanoparticles distribution around the nucleus in the cell. Although the detailed mechanism has not been clarified, such phenomenon possibly resulted from a non-specific endocytosis pathway.[63] Before the TPL imaging experiment, an excitation laser wavelength test was carried out by tuning the laser wavelength from 760 to 1000 nm. From the plot of the dependence of TPL intensity on the excitation wavelength (Figure S1 in Supporting Information), we find that the TPL intensity reaches a maximum at ~800 nm, which overlaps well with the dipolar plasmonic resonance of Fe_3O_4@SiO_2@Au nanoparticles (Figure 3A). This implies that the TPL intensity is mainly determined by the local electric field enhancement induced by the plasmon resonances for Au nanoshells. This phenomenon has also been discovered on the plasmonic nanoparticles with different shapes, such as nanorods and nanocages.[21, 32] Figure 4D shows a 2D TPL image of the same single HUVEC shown in Figure 4C excited at 800 nm, which correlates well with the distribution of nanoparticles in Figure 4C. Additionally, we took TPL images of the HUVECs without uptake of Fe_3O_4@SiO_2@Au nanoparticles as control to demonstrate the origin of the luminescence. No luminescence was detected compared to Fe_3O_4@SiO_2@Au nanoparticles-labeled HUVECs (data not shown), confirming that the luminescence was originated from Fe_3O_4@SiO_2@Au nanoparticles rather than cells themselves. Figure 4E presents a TPL 3D volume visualization of the same single cell shown in Figure 4D, which provides information of space distribution of nanoparticles in a volume image size of 212 μm × 212 μm × 30 μm.

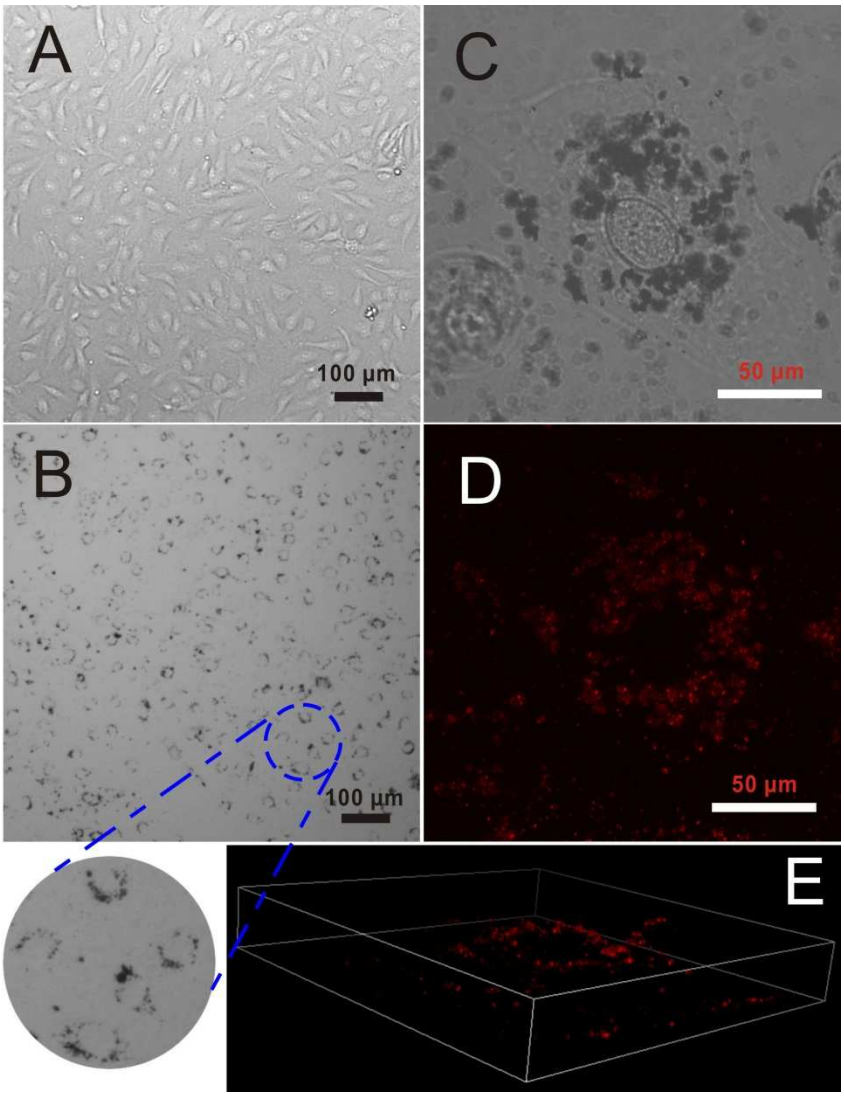

Figure 4. Bright field images of HUVECs cultured (A) without and (B) with Fe_3O_4@SiO_2@Au nanoparticles. The region in the blue circle containing several cells is magnified. (C) Transmission image, (D) 2D TPL image and (E) 3D TPL visualization of a single HUVEC labeled with Fe_3O_4@SiO_2@Au nanoparticles.

Due to the superparamagnetic property of Fe_3O_4 cores, Fe_3O_4@SiO_2@Au nanoparticles can quickly response to an external magnetic field and form parallel particle chains by a self-assembly process (see Figure S2 in Supporting Information). By combining TPL imaging with a magnetic field, we have observed that the resulted self-assembled chain structures can greatly improve the TPL intensity. Figure 5 show the TPL images of 4-MBA labeled Fe_3O_4@SiO_2@Au nanoparticles with and without the addition of an external magnetic field. When no external magnetic field was applied, the 4-MBA labeled

Fe_3O_4@SiO_2@Au nanoparticles were dispersed well in solution and no significant aggregates were formed and the TPL intensity was relatively weak (Figure 5A). In contrast, under an external magnetic field, the superparamagnetic nanoparticles were rearranged along the direction of the magnetic field and formed chains with different lengths from a few hundred nanometer to dozens of micrometer; more importantly, the TPL intensity of particles chains were greatly enhanced compared to that of separated particles without applying magnetic field (Figure 5B). Rectangle sections in Figure 5A and B were partially enlarged in Figure 5E and F, respectively, for highlighting the enhanced TPL effect of magnetic field-induced chain structures. The grayscale of each pixel along the diagonal lines in Figure 5E and F were collected and compared in Figure 5G, showing roughly one order of magnitude enhancement of TPL intensity after forming the chain structures. The origin of enhanced TPL intensity could possibly be ascribed to the near-field enhancement induced by the plasmon coupling along the chain, which promotes the two-photon excitation process.[64, 65] By tuning the external magnetic field direction, the self-assembled nanoparticle chains could respond quickly and rearrange along with the new direction of the magnetic field and the enhanced TPL effect remains (Figure 5B-D), which indicates that the TPL imaging can be used to monitor the rotation of nanoparticle chains.

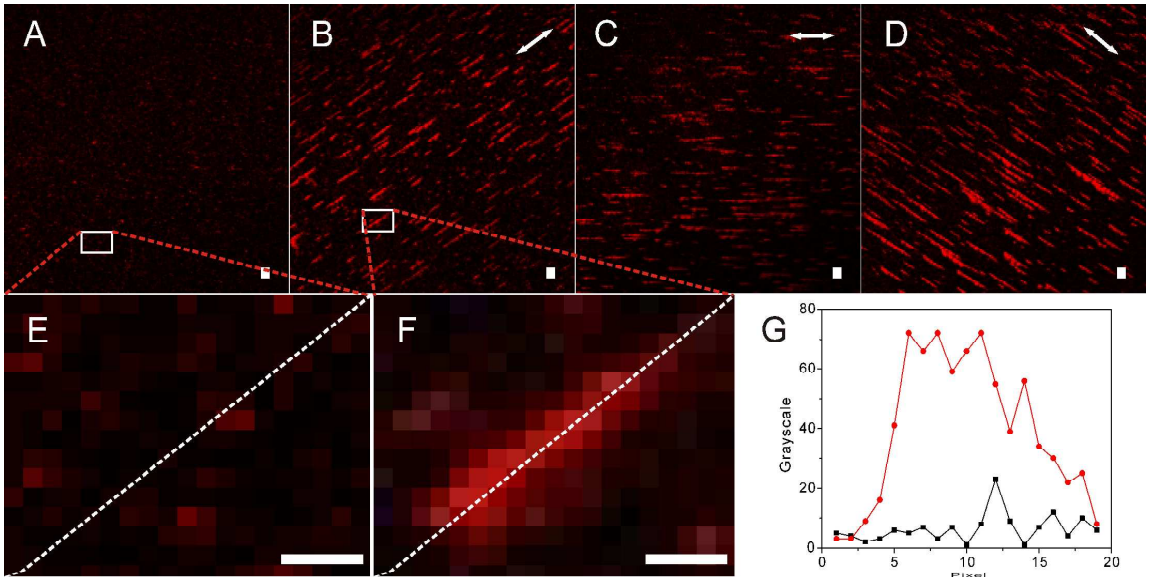

Figure 5. TPL images of 4-MBA labeled aqueous Fe_3O_4@SiO_2@Au nanoparticles applied without (A) and with an external magnetic field along the different directions (B - D). The white double-arrow symbol in (B – D) indicates the direction of the magnetic field. (E) and (F) are enlarged images of the rectangle areas as shown in panel A and B, respectively. (G) The gray-scale of each pixel along the white diagonal lines in panel E (black) and F (red). All scale bars are 10 μm.

Owing to the strong enhancement of electric fields from the dipolar plasmon resonance in the NIR region, Fe_3O_4@SiO_2@Au nanoparticles are expected to exhibit SERS effect. Herein, we employed 4-MBA molecules as a Raman reporter to evaluate the SERS performance of Fe_3O_4@SiO_2@Au nanoparticles since they can form a self-assembled monolayer on the particle surface. Figure 5 displays the remarkable difference of SERS spectra when excited by the lasers with different wavelengths. We have found strong SERS spectrum of 4-MBA molecules on Fe_3O_4@SiO_2@Au when excited by 785 nm laser, where two obvious Raman bands appeared at 1076 and 1586 cm^{-1} and were corresponding to νCS(a1) and νCC(a1) vibrational mode, respectively. Moreover, the Raman intensity at 1076 cm^{-1} is about 1.7 folds larger than that at 1586 cm^{-1}. Between these two bands, multiple weakly enhanced Raman bands at 1139, 1177, 1420 and 1479 cm^{-1} were observed, which can be assigned to the deformation vibration mode of δCH(9a) (1139 and 1177 cm^{-1}), the symmetric stretching band of

carboxylate (νCOO$^-$) and aromatic ring vibrations (δCH + νCC), respectively.[66-68] Same phenomena appeared for the excitation wavelength of 532 and 633 nm, where two of most obvious νCS(a1) and νCC(a1) vibrational modes were observed at 1076 and 1586 cm^{-1} with relatively much weaker intensities compared to ones excited by 785 nm laser. However, when the excitation wavelength was changed to 532 nm, a strong fluorescence background was detected, which is most likely arisen from the intrinsic fluorescence properties of Au nanoshells and decreases significantly when replaced by higher excitation wavelength such as 633 or 785 nm. The detailed mechanism can be illustrated as follows: at longer excitation wavelength (633 or 785 nm), the energy of incident photon is lower than the electronic transitions and the possibility of the formation of electronic excited states greatly decreased or nearly disappeared, so less fluorescence photon emit.[69] By comparing SERS spectra obtained under 532, 633 and 785 nm, superparamagnetic Fe_3O_4@SiO_2@Au nanoshells show remarkable enhancement of Raman spectrum at 785 nm. The intensity enhancement factor of Raman bands at 1076 and 1586 cm^{-1} is about 22 and 12, respectively, excited by 785 nm laser compared to that by 633 nm laser. This can be explained by the wavelength selected electric field enhancement from the dipolar plasmon resonance of superparamagnetic Fe_3O_4@SiO_2@Au nanoshells (see Figure 3C). This fact also confirms that the electromagnetic (EM) enhancement is dominant mechanism for the SERS of 4-MBA molecules on nanoshells. Additionally, it can be noticed from Figure 6 that the overall profile of SERS spectrum at each wavenumber range is similar to the shape of the extinction spectrum in the same wavelength range. We have observed similar SERS spectrum profile conversion on Au nanorings, which is due to the wavelength dependent EM effect.[70] As reported previously, magnetic-induced self-assembly could be applied to improve the intensity of SERS through the formation of hot-spots due to the plasmon coupling effect.[71, 72] We also expect that the SERS intensity can be further enhanced in the self-

assembled particle chains due to the plasmon coupling effect. The detailed work is ongoing and will be reported in the future work.

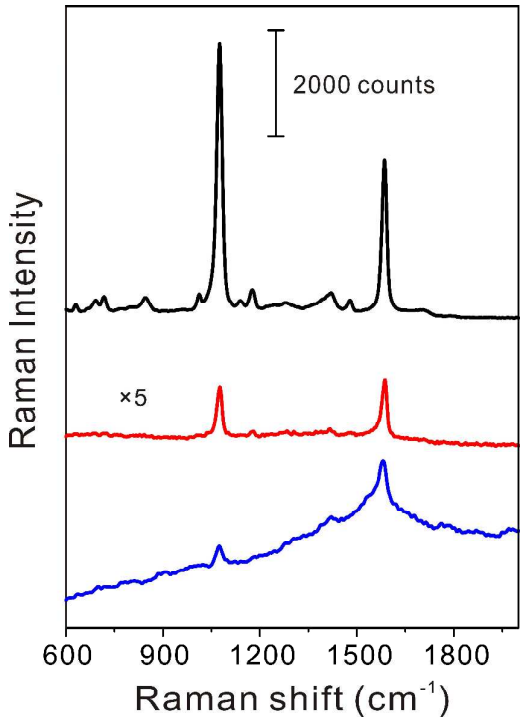

Figure 6. SERS spectra of 4-MBA decorated Fe_3O_4@SiO_2@Au nanoparticles excited by an incident laser of 785 nm (top), 633 nm (middle, with 5 times amplification of Raman intensity) and 532 nm (bottom).

In biological magnetic separation test, we trypsinized HUVECs to obtain discrete cells after culturing with superparamagnetic Fe_3O_4@SiO_2@Au nanoparticles for 24 h, and collected the superparamagnetic Fe_3O_4@SiO_2@Au labeled HUVECs by an external magnetic field of ~0.2 T. Figure 7 A-C shows the photo images before, under and after the magnetic separation process. Before magnetic separation, HUVECs took up most of superparamagnetic Fe_3O_4@SiO_2@Au nanoparticles and labeled cells were uniformly dispersed in ECM medium (Figure 7A). During the magnetic separation process, superparamagnetic Fe_3O_4@SiO_2@Au nanoparticles labeled HUVECs were quickly attached to the magnetic field side (Figure 7B) in 2 min. When the magnetic separation was completed, ECM medium

was removed and thus the Fe_3O_4@SiO_2@Au nanoparticles labeled HUVECs showing dark color can be collected (Figure 7C). Most of the nanoparticles-labeled cells can be fast and efficiently separated within 2 min with separation efficiency ranging from 50% to 88%. The obtained nanoparticles-labeled cells then can be used in other *in vitro* biological experiments. In this magnetic separation process, Fe_3O_4@SiO_2@Au nanoparticles without further surface modification were employed, showing advantages including easy preparation, fast and efficient separation. Further surface decoration may have impact on the uptake of nanoparticles by cells.[73]

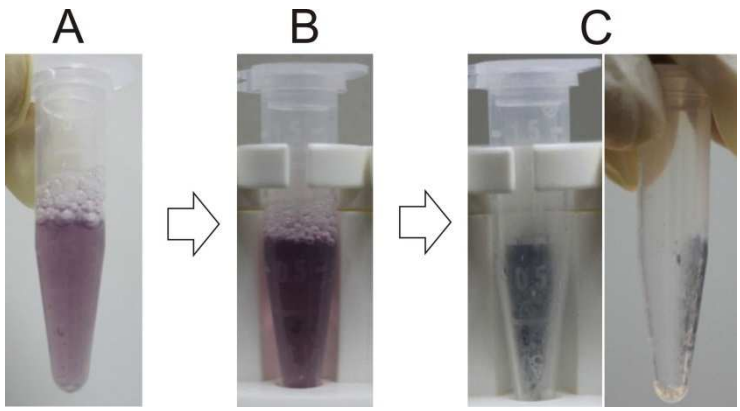

Figure 7. Optical images of Fe_3O_4@SiO_2@Au nanoparticles cultured with HUVECs (A) before, (B) under and (C) after the employment of an external magnetic field.

The combination of TPL bioimaging capability and magnetic separation renders these nanoparticles potential in many applications such as cells imaging and isolation from a cells co-culture system (e.g., HUVECs and HDFs co-culture system).[74] The aforementioned nanoparticles-labeled cells could be further manipulated or transplanted for *in vitro* or *in vivo* study. For Fe_3O_4@SiO_2@Au nanoparticles, TPL and SERS can be realized both in the NIR region. Their combination possibly allows us to in-situ monitor the variation of micro-environment (e.g., pH value) and bio-composition around nanoparticle in live cells. The observation of the TPL enhancement effect in the particle chains self-assembled under

magnetic field implies the further consideration of nanoparticles arrangement/adsorption when interacting with cells. Moreover, the possibility of continuous TPL imaging of rotational particle chains may open up new frontiers in discovering new insights into complex biological events in live cells.[75] In addition, the composition of magnetic core and Au shell in Fe_3O_4@SiO_2@Au nanoparticles offers great potential for enhanced effects on other bioimaging techniques such as magnetic resonance imaging (MRI) and computed tomography (CT).[8] Moreover, the strong plasmon resonances in NIR range from the Au shell render the extra capability of the photo thermotherapy for the tumor cells.

Conclusions

In summary, we have successfully designed and synthesized a type of multifunctional core-shell Fe_3O_4@SiO_2@Au nanoparticles, which can effectively integrate superparamagnetic and plasmonic optical properties. Experimental extinction spectrum and theoretical simulations have shown that optical properties of composite nanoparticles are mainly determined by the plasmon resonances of Au shells, which leads to their strong NIR SERS effects on 4-MBA molecules. This indicates the potential SERS-based biosensing and bioimaging capability of Fe_3O_4@SiO_2@Au nanoparticles. Using the uptake of nanoparticles by HUVECs as a convenient labeling manner, we have additionally demonstrated the TPL-based bioimaging capability of Fe_3O_4@SiO_2@Au nanoparticles in a single-cell level. By manipulating an external magnetic field, the TPL intensity could be effectively enhanced resulted from the plasmon coupling in the nanoparticle chains via a magnetic field-induced self-assembly process. Moreover, the superparamagnetic behavior of composite nanoparticles also allows for fast and efficient collection of target molecules or cells. The tri-functional combination in Fe_3O_4@SiO_2@Au nanoparticles additionally allow many potentials in the biosensing and bioimaging applications in the

intracellular level. If further accompanied by well-established surface functionalization protocols, we envision that Fe_3O_4@SiO_2@Au nanoparticles will have more potential in biomedical applications including imaging, sensing and therapy.

Acknowledgements

We gratefully acknowledge the National Natural Science Foundation of China (No. 21375087) and the Science and Technology Commission of Shanghai Municipality (No. 13ZR1422100 and14XD1402500) for their financial support.

REFERENCES

1. J. Kim, Y. Piao and T. Hyeon, *Chem. Soc. Rev.*, 2009, **38**, 372-390.
2. E. Peng, E. S. G. Choo, C. S. H. Tan, X. Tang, Y. Sheng and J. Xue, *Nanoscale*, 2013, **5**, 5994-6005.
3. E. Q. Song, J. Hu, C. Y. Wen, Z. Q. Tian, X. Yu, Z. L. Zhang, Y. B. Shi and D. W. Pang, *ACS Nano*, 2011, **5**, 761-770.
4. J. Liu, W. Zhang, H. Zhang, Z. Yang, T. Li, B. Wang, X. Huo, R. Wang and H. Chen, *Chem. Commun.*, 2013, **49**, 4938-4940.
5. M. Liong, J. Lu, M. Kovochich, T. Xia, S. G. Ruehm, A. E. Nel, F. Tamanoi and J. I. Zink, *ACS Nano*, 2008, **2**, 889-896.
6. X. B. Xiong and A. Lavasanifar, *ACS Nano*, 2011, **5**, 5202-5213.
7. D. E. Lee, H. Koo, I. C. Sun, J. H. Ryu, K. Kim and I. C. Kwon, *Chem. Soc. Rev.*, 2012, **41**, 2656-2672.
8. J. Zhu, Y. Lu, Y. Li, J. Jiang, L. Cheng, Z. Liu, L. Guo, Y. Pan and H. Gu, *Nanoscale*, 2014, **6**, 199-202.
9. Z. H. Li, Y. Tao, S. Huang, N. Gao, J. S. Ren and X. G. Qu, *Chem. Commun.*, 2013, **49**, 7129-7131.
10. C. Kaewsaneha, P. Tangboriboonrat, D. Polpanich, M. Eissa and A. Elaissari, *ACS Appl. Mater. Interfaces.*, 2013, **5**, 1857-1869.
11. P. Quaresma, I. Osorio, G. Doria, P. A. Carvalho, A. Pereira, J. Langer, J. P. Araujo, I. Pastoriza-Santos, L. M. Liz-Marzan, R. Franco, P. V. Baptista and E. Pereira, *RSC Adv.*, 2014, **4**, 3659-3667.
12. P. J. Chen, S. H. Hu, C. T. Fan, M. L. Li, Y. Y. Chen, S. Y. Chen and D. M. Liu, *Chem. Commun.*, 2013, **49**, 892-894.

13. N. Lee, H. R. Cho, M. H. Oh, S. H. Lee, K. Kim, B. H. Kim, K. Shin, T. Y. Ahn, J. W. Choi, Y. W. Kim, S. H. Choi and T. Hyeon, *J. Am. Chem. Soc.*, 2012, **134**, 10309-10312.
14. Z. Fan, M. Shelton, A. K. Singh, D. Senapati, S. A. Khan and P. C. Ray, *ACS Nano*, 2012, **6**, 1065-1073.
15. G. Chen, J. Shen, T. Y. Ohulchanskyy, N. J. Patel, A. Kutikov, Z. Li, J. Song, R. K. Pandey, H. Ågren, P. N. Prasad and G. Han, *ACS Nano*, 2012, **6**, 8280-8287.
16. R. Zhang, C. Wu, L. Tong, B. Tang and Q. H. Xu, *Langmuir*, 2009, **25**, 10153-10158.
17. J. Ando, K. Fujita, N. I. Smith and S. Kawata, *Nano Lett.*, 2011, **11**, 5344-5348.
18. J. Kneipp, H. Kneipp, B. Wittig and K. Kneipp, *Nano Lett.*, 2007, **7**, 2819-2823.
19. S. H. Nam, Y. M. Bae, Y. I. Park, J. H. Kim, H. M. Kim, J. S. Choi, K. T. Lee, T. Hyeon and Y. D. Suh, *Angew. Chem. Int. Ed.*, 2011, **123**, 6217-6221.
20. W. Denk, J. H. Strickler and W. W. Webb, *Science*, 1990, **248**, 73-76.
21. H. F. Wang, T. B. Huff, D. A. Zweifel, W. He, P. S. Low, A. Wei and J. X. Cheng, *Proc. Natl. Acad. Sci. U. S. A.*, 2005, **102**, 15752-15756.
22. J. L. Li and M. Gu, *Biomaterials*, 2010, **31**, 9492-9498.
23. J. Jiang, H. Gu, H. Shao, E. Devlin, G. C. Papaefthymiou and J. Y. Ying, *Adv. Mater.*, 2008, **20**, 4403-4407.
24. L. Tong, W. He, Y. Zhang, W. Zheng and J. X. Cheng, *Langmuir*, 2009, **25**, 12454-12459.
25. L. Tong, Q. Wei, A. Wei and J. X. Cheng, *Photochem. Photobiol.*, 2009, **85**, 21-32.
26. C. J. Murphy, T. K. Sau, A. M. Gole, C. J. Orendorff, J. Gao, L. Gou, S. E. Hunyadi and T. Li, *J. Phys. Chem. B*, 2005, **109**, 13857-13870.
27. X. F. Jiang, Y. Pan, C. Jiang, T. Zhao, P. Yuan, T. Venkatesan and Q. H. Xu, *J. Phys. Chem. Lett.*, 2013, **4**, 1634-1638.
28. D. Nagesha, G. S. Laevsky, P. Lampton, R. Banyal, C. Warner, C. DiMarzio and S. Sridhar, *Int. J. Nanomed.*, 2007, **2**, 813-819.
29. J. Park, A. Estrada, K. Sharp, K. Sang, J. A. Schwartz, D. K. Smith, C. Coleman, J. D. Payne, B. A. Korgel, A. K. Dunn and J. W. Tunnell, *Opt. Express*, 2008, **16**, 1590-1599.
30. J. Park, A. Estrada, J. A. Schwartz, P. Diagaradjane, S. Krishnan, A. K. Dunn and J. W. Tunnell, *Laser. Surg. Med.*, 2010, **42**, 630-639.
31. L. Bickford, J. Sun, K. Fu, N. Lewinski, V. Nammalvar, J. Chang and R. Drezek, *Nanotechnology*, 2008, **19**, 315102.
32. L. Au, Q. Zhang, C. M. Cobley, M. Gidding, A. G. Schwartz, J. Y. Chen and Y. N. Xia, *ACS Nano*, 2010, **4**, 35-42.
33. L. Gao, J. B. Fei, J. Zhao, H. Li, Y. Cui and J. B. Li, *ACS Nano*, 2012, **6**, 8030-8040.
34. L. Tong, C. M. Cobley, J. Chen, Y. Xia and J. X. Cheng, *Angew. Chem. Int. Ed.*, 2010, **49**, 3485-3488.
35. W. Choi, A. Sahu, Y. Kim and G. Tae, *Ann. Biomed. Eng.*, 2012, **40**, 534-546.
36. J. L. Li, H. C. Bao, X. L. Hou, L. Sun, X. G. Wang and M. Gu, *Angew. Chem. Int. Ed.*, 2012, **51**, 1830-1834.
37. A. J. Coughlin, J. S. Ananta, N. Deng, I. V. Larina, P. Decuzzi and J. L. West, *Small*, 2014, **10**, 556-565.
38. B. Yan and B. M. Reinhard, *J. Phys. Chem. Lett.*, 2010, **1**, 1595-1598.
39. Y. Liu and P. Wu, *ACS Appl. Mater. Interfaces.*, 2013, **5**, 5832-5844.
40. A. Huefner, W. L. Kuan, R. A. Barker and S. Mahajan, *Nano Lett.*, 2013, **13**, 2463-2470.
41. Z. Gan, A. Zhao, M. Zhang, W. Tao, H. Guo, Q. Gao, R. Mao and E. Liu, *Dalton. T.*, 2013, **42**,

8597-8605.
42. Z. Y. Bao, D. Y. Lei, R. Jiang, X. Liu, J. Dai, J. Wang, H. L. W. Chan and Y. H. Tsang, *Nanoscale*, 2014, **6**, 9063-9070.
43. W. Cai, X. Tang, B. Sun and L. Yang, *Nanoscale*, 2014, **6**, 7954-7958.
44. S. W. Bishnoi, C. J. Rozell, C. S. Levin, M. K. Gheith, B. R. Johnson, D. H. Johnson and N. J. Halas, *Nano Lett.*, 2006, **6**, 1687-1692.
45. A. Barhoumi and N. J. Halas, *J. Am. Chem. Soc.*, 2010, **132**, 12792-12793.
46. M. Ochsenkühn and C. Campbell, in *Raman Spectroscopy for Nanomaterials Characterization*, ed. C. S. R. Kumar, Springer Berlin Heidelberg, 2012, DOI: 10.1007/978-3-642-20620-7_3, ch. 3, pp. 51-74.
47. Y. Huang, V. P. Swarup and S. W. Bishnoi, *Nano Lett.*, 2009, **9**, 2914-2920.
48. A. Barhoumi and N. J. Halas, *J. Phys. Chem. Lett.*, 2011, **2**, 3118-3123.
49. J. Ge, Y. Hu and Y. Yin, *Angew. Chem. Int. Ed.*, 2007, **46**, 7428-7431.
50. F. J. Xu, C. M. Cheng, D. X. Chen and H. C. Gu, *ChemPhysChem*, 2012, **13**, 336-341.
51. J. Ge, Y. Hu, T. Zhang and Y. Yin, *J. Am. Chem. Soc.*, 2007, **129**, 8974-8975.
52. D. G. Duff, A. Baiker and P. P. Edwards, *Langmuir*, 1993, **9**, 2301-2309.
53. B. E. Brinson, J. B. Lassiter, C. S. Levin, R. Bardhan, N. Mirin and N. J. Halas, *Langmuir*, 2008, **24**, 14166-14171.
54. E. A. Jaffe, R. L. Nachman, C. G. Becker and C. R. Minick, *J. Clin. Invest.*, 1973, **52**, 2745-2756.
55. J. Ye, N. Verellen, W. Van Roy, L. Lagae, G. Maes, G. Borghs and P. Van Dorpe, *ACS Nano*, 2010, **4**, 1457-1464.
56. X. P. Fang, Y. M. Xuan and Q. Li, *Nanoscale Res. Lett.*, 2011, **6**.
57. Q. Zhang, J. Ge, J. Goebl, Y. Hu, Y. Sun and Y. Yin, *Adv. Mater.*, 2010, **22**, 1905-1909.
58. S. J. Oldenburg, G. D. Hale, J. B. Jackson and N. J. Halas, *Appl. Phys. Lett.*, 1999, **75**, 1063-1065.
59. J. Ye, P. Van Dorpe, W. Van Roy, K. Lodewijks, I. De Vlaminck, G. Maes and G. Borghs, *J. Phys. Chem. C*, 2009, **113**, 3110-3115.
60. P. Swanglap, L. S. Slaughter, W. S. Chang, B. Willingham, B. P. Khanal, E. R. Zubarev and S. Link, *ACS Nano*, 2011, **5**, 4892-4901.
61. J. Ye, M. Shioi, K. Lodewijks, L. Lagae, T. Kawamura and P. Van Dorpe, *Appl. Phys. Lett.*, 2010, **97**.
62. S. J. Oldenburg, R. D. Averitt, S. L. Westcott and N. J. Halas, *Chem. Phys. Lett.*, 1998, **288**, 243-247.
63. X. Nie, J. Zhang, Q. Xu, X. Liu, Y. Li, Y. Wu and C. Chen, *J. Mater. Chem. B*, 2014, **2**, 3232-3242.
64. Z. Guan, L. Polavarapu and Q. H. Xu, *Langmuir*, 2010, **26**, 18020-18023.
65. F. Han, Z. Guan, T. S. Tan and Q. H. Xu, *ACS Appl. Mater. Interfaces.*, 2012, **4**, 4746-4751.
66. C. J. Orendorff, A. Gole, T. K. Sau and C. J. Murphy, *Anal. Chem.*, 2005, **77**, 3261-3266.
67. A. Weigel and N. P. Ernsting, *J. Phys. Chem. B*, 2010, **114**, 7879-7893.
68. K. W. Kho, U. S. Dinish, A. Kumar and M. Olivo, *ACS Nano*, 2012, **6**, 4892-4902.
69. K. A. Christensen, E. A. Todd and M. D. Morris, in *Kirk-Othmer Encyclopedia of Chemical Technology*, John Wiley & Sons, Inc., 2000, DOI: 10.1002/0471238961.1801130103081809.a01, pp. 1-14.
70. J. Ye, J. A. Hutchison, H. Uji-i, J. Hofkens, L. Lagae, G. Maes, G. Borghs and P. Van Dorpe,

Nanoscale, 2012, **4**, 1606-1611.
71. L. Polavarapu and Q. H. Xu, *Langmuir*, 2008, **24**, 10608-10611.
72. Z. Y. Bao, J. Dai, D. Y. Lei and Y. Wu, *J. Appl. Phys.*, 2013, **114**, 124305.
73. L. A. Dykman and N. G. Khlebtsov, *Chem. Rev.*, 2013, **114**, 1258-1288.
74. H. Li and J. Chang, *Acta Biomater.*, 2013, **9**, 6981-6991.
75. G. Wang, A. S. Stender, W. Sun and N. Fang, *Analyst*, 2010, **135**, 215-221.